Investigation of inner-outer interactions in a turbulent boundary layer using time-resolved PIV

Gokul Pathikonda

Department of Mechanical Science and Engineering
University of Illinois, Urbana-Champaign, USA
Department of Aerospace and Mechanical Engineering
University of Notre Dame, IN, USA

Kenneth T Christensen

Aerospace and Mechanical Engineering &
Civil and Environmental Engineering and Earth Sciences
University of Notre Dame, IN, USA
christensen.33@nd.edu

ABSTRACT

Experiments were performed in a refractive-index-matching (RIM) flow facility to investigate inner–outer interactions over smooth and rough walls using time-resolved PIV. Lack of near-wall reflections due to RIM enabled measurements very close to the smooth and rough surfaces using PIV. Two cameras, with different fields of view and spatial resolutions, were used to view the streamwise–wall normal plane. Measurements of the smooth-wall boundary layer display amplitude and frequency modulations similar to those reported in the literature. Further, conditional averages were used to evaluate the spatio-temporal evolution of the large-scale influences on the small scales, and their influences on energy distributions of the small-scale turbulence. The observations from the conditional averages yielded a picture consistent with the hot-wire measurements reported in the literature. The smooth-wall measurements and analysis described in the current work established the phenomena and analytical tools to extend the current techniques to better understand roughness effects.

INTRODUCTION

A high Reynolds number (Re) smooth wall boundary layer can be broadly divided into three physical regions – a near-wall region, an inertial layer and a wake region. The near-wall region embodies the turbulence production cycle, where the high shear results in much of the turbulence production. It is populated by smaller-scale, streamwise oriented coherent structures that result in the well known near-wall turbulent kinetic energy peak at viscous scaled streamwise wavelengths around $O(10^3)$. Far away from the wall, the wake region consists of turbulent bulges inclined in the streamwise direction, and is very intermittent due to patches of free stream fluid (high momentum, low turbulence) being entrained, and the turbulent fluid (low momentum, high turbulence) being ejected. In between sits an equilibrium region, termed the inertial/overlap region, which embodies a cascade of scales transferring the free stream momentum to the near-wall region and near-wall turbulence away from the wall.

The inertial region has been found (Kim & Adrian, 1999) to contain large- and very large-scale motions (LSMs and VLSMs) that scale with outer variables, and thus become increasingly stronger with Re. It can be speculated that that at high Re, these outer layer structures exhibit an increasing influence on the near-wall dynamics. Early observations by Rao *et al.* (1971) and Bandyopadhyay & Hussain (1984) have indicated the same. More recently, it was found that these outer-layer superstructures exhibit a modulating influence on the near-wall structures, termed inner–outer interactions. Amplitude and frequency modulations of the near-wall scales by the outer-layer structures have been reported smooth-wall flow at high Re (e.g. Mathis *et al.*, 2009; Baars *et al.*, 2015). The same has also been observed in DNS and LES of smooth-wall turbulent boundary layers (Bernardini & Pirozzoli, 2011; Anderson, 2016). Interesting interpretations, such as Quasi-steady – Quasi homogenous nature of the near-wall turbulence, have been proposed to explain these interactions (Hutchins, 2014; Zhang & Chernyshenko, 2016). Further, models to accurately account for amplitude modulation phenomena, and predict various quantities such as velocity spectra and wall shear stress fluctuations have been proposed (e.g. Mathis *et al.*, 2011*a*).

With these recent developments in our understanding of smooth-wall turbulence, it is a logical question to investigate the same in rough-wall flows. It is accepted that at high Re, a rough wall boundary layer that is thick relative to the roughness height exhibits outer-layer similarity, meaning that the outer-layer structure is similar to that of the smooth-wall flow, though the the near-wall production cycle is now replaced by a roughness sublayer where viscous effects can be minimal. Our previous work has clearly shown the presence of both amplitude and frequency modulation in a rough-wall turbulent boundary layer with a multi-scale roughness topography (Pathikonda & Christensen, 2017). Further, LES computations over rough-wall flows have also indicated similar phenomenon (Anderson, 2016). In view of this new information about inner–outer interactions over rough-wall flows, it is of interest to explore these phenomena in greater detail in rough-wall flows. We aim to investigate them using a combination of time-resolved PIV in a refractive index matching flow facility.

EXPERIMENTS

All the experiments in the current work are performed in the refractive index matching (RIM) facility in the Turbulence Laboratory for Energy and the Environment (LTE^2) at the University of Notre Dame. The facility is a water tunnel with 63% concentrated Sodium Iodide (NaI) solution as the working fluid. The refractive index of the solution can be closely controlled and adjusted to match that of the wall and the roughness (cast using clear acrylic with $RI \sim 1.499$), to render them optically invisible. Doing so reduces the near-wall laser light reflections and enables investigation very close to the wall using optical techniques such as PIV. This is particularly useful when investigating inner–outer interactions, since, as shown in earlier studies (Mathis *et al.*, 2009; Pathikonda & Christensen, 2017; Baars *et al.*, 2015, among others), much of the modulation interactions occur very close to the wall where the turbulent scales are rich and small enough to be modulated by the very large scales in the outer region.

The PIV arramgement consists of two high-speed Phantom V641 4MP CMOS cameras, operating synchronously, with a configuration shown in Figure 1. They are used to simultaneously view two different fields of view (FOV) from opposite sides of the light sheet, with different magnifications to suit the resolution requirements imposed by the turbulent flow. The near-wall camera (*Camera-1*, sFOV) investigates flow in the immediate vicinity of the wall, has FOV dimensions of ($\approx$40 mm $\times$ 25 mm) in streamwise – wall-normal directions and captures small scales near the wall with high spatial resolution. The second camera (*Camera-2*, bFOV)

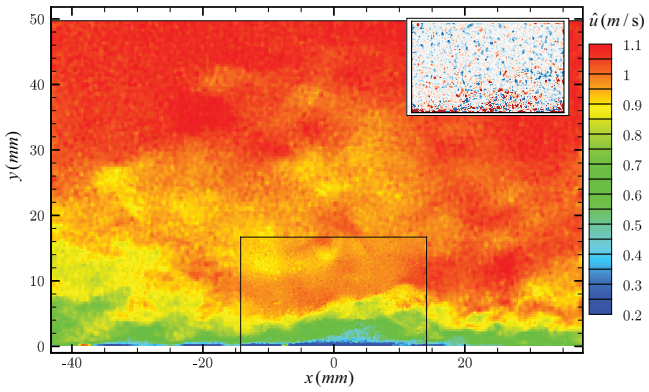

Figure 1. An example instantaneous snapshot of streamwise velocity contours from the two cameras. The small camera (sFOV) is embedded inside the big camera near the wall. Also shown in inset is the velocity difference between the two cameras (contours ranging from -0.04 m/s to 0.04 m/s).

has FOV dimensions (≈80 mm × 50 mm) in the streamwise – wall-normal directions and captures boundary layer parameters and large scales away from the wall that are longer in streamwise direction. The two FOVs are arranged as shown in Figure 1. The cameras make synchronous acquisition of PIV images at 700 image-pairs per second. The light sheet is illuminated by a Northrop Grumman Patara Nd–YLF laser with an energy of 50 mJ/pulse/head and $2\mu m$ silver coated solid glass spheres were used for seeding the flow.

Acquisition was performed at 700 vector fields per second, which, with the current camera internal memory, gives a time series about 3.9 s long (2700 time-resolved vector fields). The current boundary layer has a free stream velocity of 1.07 m/s and a boundary layer thickness of about 40 mm, which gives a Kármán number, or Reynolds number based on inner scaling (Re_τ), of around 1400. Thus, each PIV time series captured is about about $110\,\delta$ long (using Taylor's hypothesis). Twenty sets of time series in each camera are acquired for the smooth-wall flow, giving an equivalent data of $2200\,\delta$ for statistical convergence of quantities, along with one set of low frame rate data (20 vector fields per second) to compute the boundary-layer parameters. This smooth-wall data was used to verify the observations with previous studies, and a baseline against which the planned rough-wall measurements and results are to be compared.

A sample vector field is shown in Figure 1 that indicates the quality of the measurements over the smooth-wall flow. The differences in the resolution can be seen clearly. Figure 1 also shows the difference in the measured velocities within the overlapped region by the two independent cameras. The deviation between the two cameras is less than 0.08 m/s (with a 1 m/s free stream velocity), highlighting the quality of the measurements.

MEAN VELOCITY CHARACTERISTICS

Using the low frame rate data, mean and turbulent statistics of the smooth-wall boundary layer was calculated by first ensemble averaging, and then line averaging in streamwise direction. The boundary layer parameters were found using a parametric non-linear regression fit to a theoretical form Chauhan *et al.* (2007). Figure 2 shows the turbulent boundary layer profiles, compared with DNS ($\mathrm{Re}_\tau = 1270$) and experimental data ($\mathrm{Re}_\tau = 1400$) at comparable Re_τ reported in literature (Schlatter & Örlü, 2010; Örlü & Schlatter, 2013). The wake of the current flow appears weaker than that of the canonical boundary layer as there exists a slight favorable gradient in the RIM facility. Since much of the inner–outer interactions occur close to the wall and in the inertial region, we expect this wake to not significantly affect the conclusions in the current work related to the modulation interaction dynamics. Further, the in-plane Reynolds stresses and the skewness of streamwise velocity agree well with the literature. Table 1 summarizes the experimental details and boundary layer parameters for the current smooth-wall flow.

Table 1. Experimental Parameters

Quantity	Symbol	Parameter
Kárṁan Number	Re_τ	1410
Free Stream Velocity	U_∞	1.07 m/s
Boundary layer thickness	δ	38.3 mm
Viscous length scale	y^*	27.1 μm
Temporal resolution	Δt	$2.35y^*/u_\tau$
Length of time series	T	$109\,\delta/U_\infty$

Figure 3 shows the pre-multiplied spatial spectrum of streamwise ($k_x\phi_{uu}$) and wall-normal ($k_x\phi_{vv}$) turbulent kinetic energy from the bFOV, giving the distribution of energy among various log-spaced scales (the integral of the same at all wavelengths recovers the streamwise/wall-normal turbulence shown in figure 2). A near-wall peak at $y^+ \approx 15$ and $\lambda_x^+ \approx 1000$ is seen in the streamwise turbulent kinetic energy component, as expected, which reflects the expected near-wall turbulence production cycle. Temporal spectra (using Taylor's hypothesis) and spatial spectra from the sFOV indicate identical distributions, and are not shown here for brevity.

TEMPORAL-ONLY MODULATION ANALYSIS

Before investigating the spatio–temporal physics of the inner–outer interactions, a preliminary understanding of the flow can be obtained by simply extracting the temporal evolution at a fixed grid point in the PIV data. Doing so is equivalent to an array of 2-component hot-wire probes making temporal measurements. Amplitude and frequency modulation is first established using similar methods established previously by various studies, such as Mathis *et al.* (2009, 2011*a*), Baars *et al.* (2015) and Bernardini & Pirozzoli (2011), for example, and provides the first evidence of correlations between the large and small scales, particularly the correlation between the former and the amplitude and frequency changes of the latter. Further, using the same metrics and the two-component time-series, the modulation interactions on the wall-normal component can also be investigated. The current section demonstrates the identification of inner–outer interactions using PIV based on these metrics. Thus, 'large' and 'small' in the current section implies 'fast' and 'slow' evolution, respectively, of the time-series in question, and not their spatial variations as captured by PIV. This latter analysis will be considered in the next section. Results from the uncorrelated time-series sections are ensemble averaged for all statistics considered.

Amplitude Modulation

Many past studies have used various techniques to investigate the amplitude modulation of the small scales by the large scales. All of these metrics involve first filtering the large ('slow') scales from the small ('fast') scales. These filtered large-scale fluctuations are correlated with variations in envelope of the small scales (Mathis

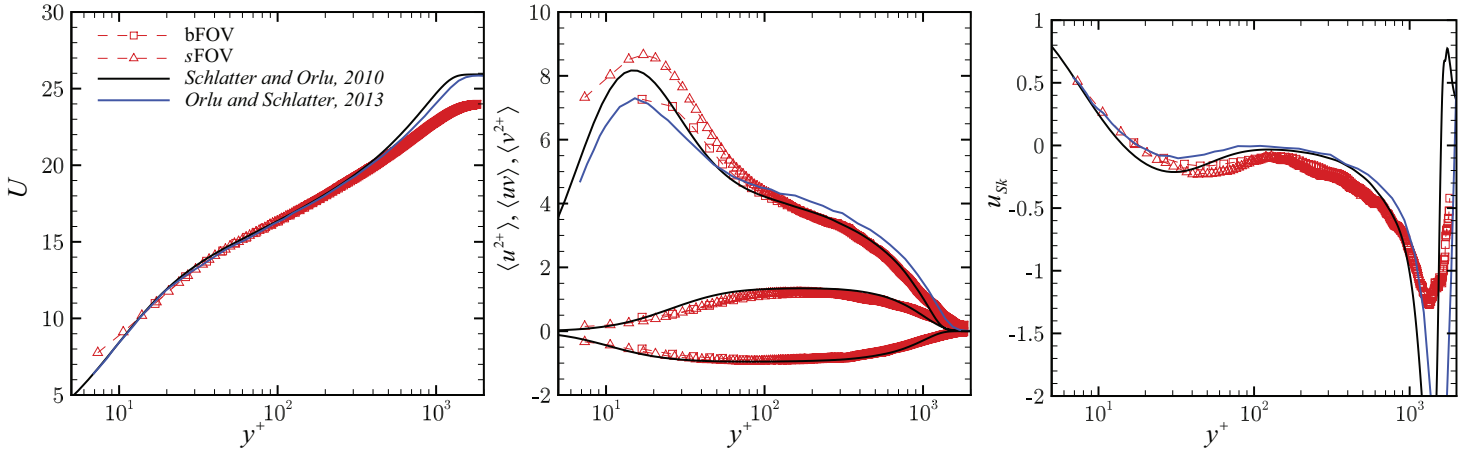

Figure 2. Mean velocity and turbulence statistics from low-frame rate PIV datasets. bFOV and sFOV refer to results from big- and small-FOV cameras, respectively.

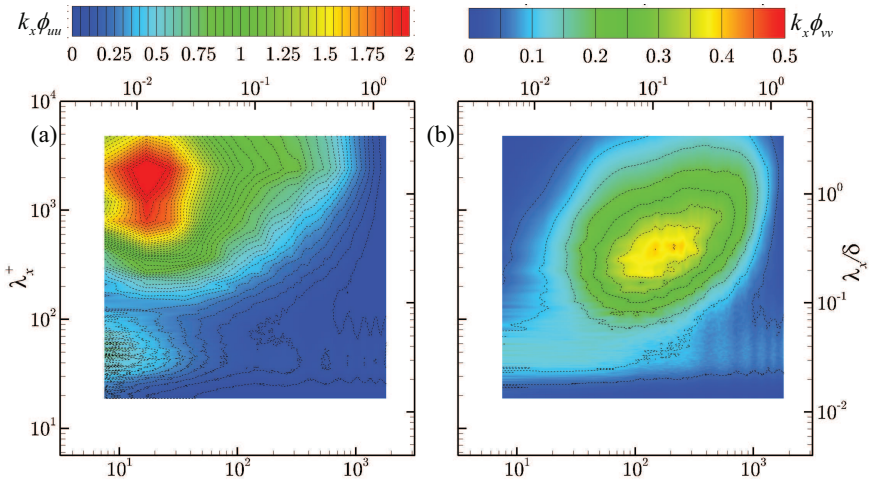

Figure 3. Premultiplied spatial spectrum of (a) streamwise and (b) wall-normal turbulent kinetic energy (from bFOV).

et al., 2009; Pathikonda & Christensen, 2017, etc.), magnitude of small scales (Bandyopadhyay & Hussain, 1984; Guala *et al.*, 2011), variance of small scales (Ganapathisubramani *et al.*, 2012), small-scale wavelet energy (Baars *et al.*, 2015), etc. Amplitude modulation of the near-wall scales were established in the current canonical flow using the large scale envelope of the small-scale fluctuations employed in Mathis *et al.* (2009), and the small scale wavelet energy fluctuations employed in Baars *et al.* (2015). Further, the large scales can be sampled at the same location ('single-point' analysis), or in the logarithmic region ('two-point' analysis). The former assumes that the large scales linearly superpose on the near-wall scales, while the latter independently measures the inertial region large scales. The latter analysis is a more direct measure of modulation influences, particularly at low-Re (Bernardini & Pirozzoli, 2011) and in flows over roughness where such assumptions of superposition are not justified *a priori*. A cut-off wavelength (λ_c) of $1\,\delta$ was used for the current analysis and the large-scale signal used throughout is based on the streamwise velocity component.

Figure 4 shows the amplitude modulation correlation coefficient in *u*- and *v*- velocity fluctuations from single-point and two-point analysis using the two metrics described above. The amplitude modulation close to the wall is evident in the *u*- and *v*- correlation coefficients from the high correlation values between the large- and small-scale energy variations. Both the wavelet-integral and large-scale envelope methods give identical results for the amplitude modulation correlation coefficient of both velocity components. These results agree well with the conclusions drawn in Talluru *et al.* (2014), who investigated amplitude modulation of all three velocity components using hot-wire measurements.

Frequency Modulation

Similar to amplitude modulation, frequency modulation investigates the modification of small-scale frequency changes to the large-scale velocity variations in the log region. This analysis can be accomplished either via peak-counting and conditional averaging (Ganapathisubramani *et al.*, 2012) or using the wavelet power spectrum (WPS, Baars *et al.* (2015)). The current study uses the latter approach, where an instantaneous frequency (f_s) is defined as the first moment of the wavelet energy distribution at various frequencies at a given time instant. The procedure for calculating the various correlation coefficients is similar to that of amplitude modulation in the previous section, except that one now correlates large scales with instantaneous frequency, instead of the envelope. More details of this method can be found in Baars *et al.* (2015). It was noted in previous studies (Pathikonda & Christensen, 2017) that the frequency modulation is a 'cleaner' measure of inner–outer interactions compared to amplitude modulation owing to the susceptibility of the latter to capture the inertial-region scale arrangement, and

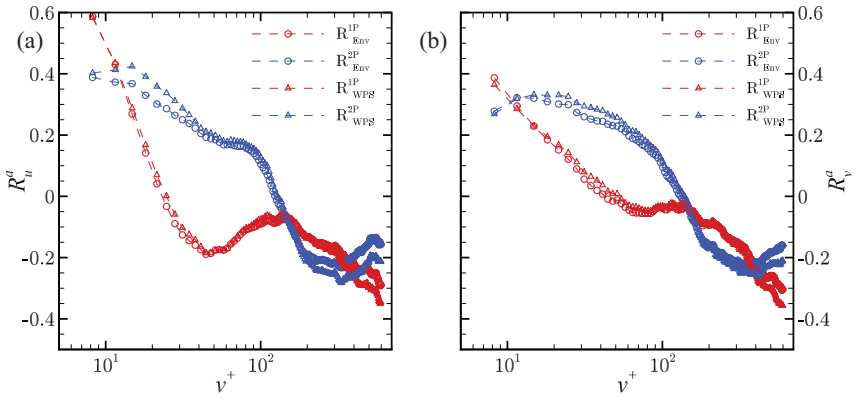

Figure 4. Single-point (red) and two-point (blue) amplitude modulation correlation coefficients of (a) streamwise and (b) wall-normal velocities using the large-scale envelope (◯) and wavelet transform (△) methods.

thus 'cloud' the true near-wall amplitude modulation peak.

Figure 5 presents the correlation coefficients of frequency modulation of near-wall small scales in u and v velocity fluctuations using one-point and two-point analysis. These results are similar to those presented in figure 4 for amplitude modulation. The correlation peak of frequency modulation in u near the wall is weak compared to amplitude modulation and the frequency modulation coefficients reported in the literature for smooth-wall flow. This difference could be due to two reasons. First, the Re_τ of the current study is much lower than other studies on smooth-wall boundary layers (Baars *et al.*, 2015; Pathikonda & Christensen, 2017). Since the modulation effects are strongly related to the Re of the boundary layer (Mathis *et al.*, 2009, 2011*b*) , these effects are inherently weaker in the current flow. Second, the wavelet power spectrum, and the instantaneous frequency, has been found to be very sensitive to noise. The PIV measurements, particularly very close to the wall, are more susceptible to noise than the corresponding hot-wire measurements owing to various factors such as low seeding density, high shear, low mean displacements and sub-pixel approximation, etc. This effect is more severe in the wall-normal velocity measurements, which are small in magnitude and thus have a lower signal-to-noise ratio due to random noise from sub-pixel approximation compared to the u velocity component. This effect can be seen in decreasing correlation coefficient in the wall-normal velocity. Nevertheless, frequency modulation of the near-wall small scales by the outer-layer large scales is still noted in both the u and v velocities.

ZERO-CROSSING CONDITIONAL AVERAGES

Besides correlations, the modulation interactions can also be investigated using conditional averaging of small-scale properties with those of the large scales. By conditioning the large-scale events and averaging, the spatial signatures of the inner–outer interactions can also be captured using the time-resolved PIV data, along with their temporal evolution. Doing so leverages the *spatial* information captured within the PIV FOV and thus provides even richer information on the spatial characteristics of these interactions than previously reported hot-wire measurements.

For this purpose, it is necessary to determine a specific condition of the large scales for which an average can then be defined. This process is similar to the conditional averages explored in Baars *et al.* (2015). The conditional event considered herein is the *positive zero-crossing of the large scale at the center of logarithmic region*. The following steps explain the conditional averaging procedure:

1. The large-scale evolution of the streamwise velocity, u_{oL}, is extracted at the geometric center of the logarithmic region given by $y_o = \sqrt{15 Re_\tau}$ (Ng *et al.*, 2011), and at a prescribed $x_o = 0$.
2. The instances $\tau^i_{0^+}(i = 1, 2..n)$ where the large scale crosses from negative to positive (with time, t) are identified. These instances are referred to as the "positive zero-crossings (τ_{o^+})" of the large-scale structure, and form the conditional events for the current analysis.
3. The zero-conditioned ensembles of the velocity fields in bFOV and sFOV are formed by collecting the velocity vector fields as

$$u|_{o^+} = [u(x, y, \tau_{o^+} + \tau)]_{\tau^i_{0^+}} . \tag{1}$$

The $u|_{o^+}$ ensembles around an interval (τ) from $-100y^*/u_\tau$ to $100y^*/u_\tau$ relative to τ_{0^+} are formed.
4. The large- and small-scale fluctuations are calculated as

$$[u|_{o^+}]_L = \langle u|_{o^+} \rangle \tag{2}$$
$$[u|_{o^+}]_s = u|_{o^+} - [u|_{o^+}]_L \tag{3}$$

where $\langle \cdot \rangle$ denotes ensemble averaging.
5. The ensemble-averaged small-scale variance, $\langle [u|_{o^+}]^2_s \rangle$, is computed, and the evolution of this small-scale variance with the large scales can be visualized by the conditional averaging.
6. Finally, the discrepancy in small-scale variance, $\Delta\langle [u|_{o^+}]^2_s \rangle$, is computed as the difference between the conditional quantity and the unconditional small-scale variance. This discrepancy clearly indicates if any correlated changes occur relative to the large scales.

$$\Delta\langle [u|_{o^+}]^2_s \rangle = \langle [u|_{o^+}]^2_s \rangle - \langle [u]^2_s \rangle. \tag{4}$$

Figure 6 shows the conditionally-averaged field of the large-scale fluctuations $[u|_{o^+}]_L$ at the instant ($\tau_\downarrow$) corresponding to a low-momentum event. For reference, the high-momentum event occurs at a delay $\tau_\uparrow \approx 50y^*/u_\tau$ after the occurrence zero-crossing event, and the low-momentum event occurs at $\tau_\downarrow \approx -50y^*/u_\tau$ before the same. By comparing this conditionally-averaged event, the corresponding small-scale variance ($\langle [u|_{o^+}]^2_s \rangle$, not shown here) and discrepancies ($\Delta\langle [u|_{o^+}]^2_s \rangle$), the effect of the large scales on the small scales can be clearly discerned. As shown in figure 6, the low-momentum event correlates well with a decrease in near-wall tur-

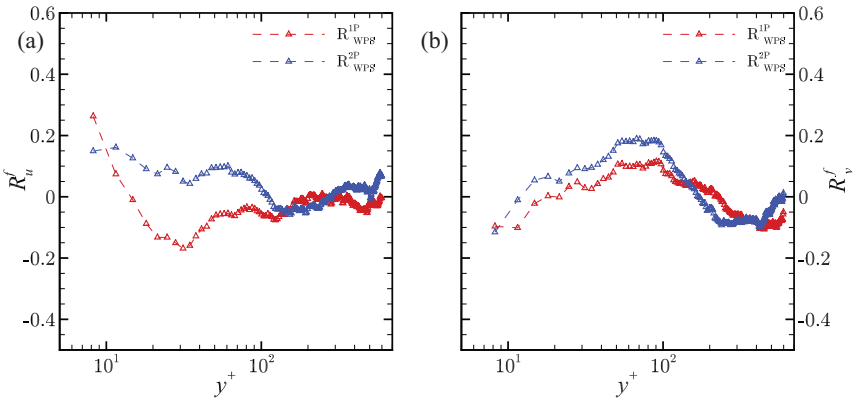

Figure 5. Single-point (red) and two-point (blue) freqeuncy modulation correlation coefficients of (a) streamwise and (b) wall-normal velocities.

bulence small-scale energy (negative discrepancy). Similarly, high-momentum event correlates well with an increase in small-scale energy (positive discrepancy, not shown here). Further, the associated increase/decrease in the near-wall turbulence occurs at a later time than the high-momentum, large-scale event in the log region. This observation is consistent with previous observations in the literature (Pathikonda & Christensen, 2017; Chung & McKeon, 2010; Baars *et al.*, 2015, for example). Similar observations were made with the wall-normal component as well.

Using this conditional averaging approach, the average streamwise turbulent spectra and the associated correlations with the large-scale event away from the wall can be investigated. Figure 7 shows the discrepancy in energy spectra ($\Delta[\langle k_x \phi_{uu} \rangle_{o^+}]$) with time delay from the zero-crossing event, τ, at a wall-normal location in the buffer region ($y^+ \approx 21$). As expected, there is an increase in the overall turbulent energy peak with respect to the large-scale event. There also appears to be indicators of streamwise turbulent scale modulation, where the discrepancy peak shifts towards smaller scales with the high-momentum event ($\tau_\uparrow$) and towards large scales with a low-momentum event ($\tau_\downarrow$). This behavior, however, could also be an artifact of insufficient convergence of the spectra, and requires a larger conditional ensemble or smoother spectrum to more definitively establish such a phenomenon.

CONCLUSIONS

Time resolved PIV measurements were made using a dual-camera PIV system to investigate inner–outer interactions in a refractive index matching flow facility. The first camera had a smaller field of view and higher spatial resolution to resolve the near-wall scales, while the second camera had a large field of view to capture the longer streamwise velocity scales away from the wall. The high spatial and temporal resolution of the system was used to evaluate the inner–outer interactions present in smooth-wall turbulence, and develop spatio–temporal tools for the investigation of the same over rough walls. The presence of amplitude and frequency modulation was demonstrated using correlation-based and temporal-only point analysis, typical of analyses using hot-wire data. While the amplitude modulation was shown as expected, the frequency modulation was more difficult to effectively capture using a PIV system due to finite measurement volume (compared to hot-wire), and increased susceptibility to noise of the frequency modulation correlation coefficient. Finally, conditional averaging indicated the time evolution of the inner–outer interactions, and a spatial description consistent with past hot-wire observations.

This work is supported by the Air Force Office of Scientific Research, under Grant No. FA9550-14-1-0101 (Dr. Douglas Smith, Program Manager). The authors also thank Caitlyn Clark for her assistance in conducting the experiment.

REFERENCES

Anderson, W. 2016 Amplitude modulation of streamwise velocity fluctuations in the roughness sublayer: evidence from large-eddy simulations. *J. Fluid Mech.* **789**, 567–588.

Baars, W.J., Talluru, K.M., Hutchins, N. & Marusic, I. 2015 Wavelet analysis of wall turbulence to study large-scale modulation of small scales. *Exp. Fluids* **56** (10), 1–15.

Bandyopadhyay, P. R. & Hussain, A.K.M.F. 1984 The coupling between scales in shear flows. *Phys. Fluids* **27** (9), 2221–2228.

Bernardini, M. & Pirozzoli, S. 2011 Inner/outer layer interactions in turbulent boundary layers: a refined measure for the large-scale amplitude modulation mechanism. *Phys. Fluids* **23** (6), 061701.

Chauhan, K., Nagib, H. & Monkewitz, P. 2007 On the composite logarithmic profile in zero pressure gradient turbulent boundary layers. In *Proc. 45th AIAA Aerospace Sciences Meeting, Paper No. AIAA*, , vol. 532, pp. 1–18.

Chung, D. & McKeon, B.J. 2010 Large-eddy simulation of large-scale structures in long channel flow. *J. Fluid Mech.* **661**, 341–364.

Ganapathisubramani, B., Hutchins, N., Monty, J.P., Chung, D. & Marusic, I. 2012 Amplitude and frequency modulation in wall turbulence. *J. Fluid Mech.* **712**, 61–91.

Guala, M., Metzger, M. & McKeon, B.J. 2011 Interactions within the turbulent boundary layer at high reynolds number. *J. Fluid Mech.* **666**, 573–604.

Hutchins, N. 2014 Large-scale structures in high reynolds number wall-bounded turbulence. In *Progress in Turbulence V*, pp. 75–83. Springer.

Kim, K.C. & Adrian, R.J. 1999 Very large-scale motion in the outer layer. *Phys. Fluids* **11** (2), 417–422.

Mathis, R., Hutchins, N. & Marusic, I. 2009 Large-scale amplitude modulation of the small-scale structures in turbulent boundary layers. *J. Fluid Mech.* **628**, 311–337.

Mathis, R., Hutchins, N. & Marusic, I. 2011*a* A predictive inner–outer model for streamwise turbulence statistics in wall-bounded flows. *J. Fluid Mech.* **681**, 537–566.

Mathis, R., Marusic, I., Hutchins, N. & Sreenivasan, K.R. 2011*b* The relationship between the velocity skewness and the amplitude modulation of the small scale by the large scale in turbulent boundary layers. *Phys. Fluids* **23** (12), 121702.

Ng, H.C.H., Monty, J.P., Hutchins, N., Chong, M.S. & Marusic, I. 2011 Comparison of turbulent channel and pipe flows with varying Reynolds number. *Exp. Fluids* **51** (5), 1261–1281.

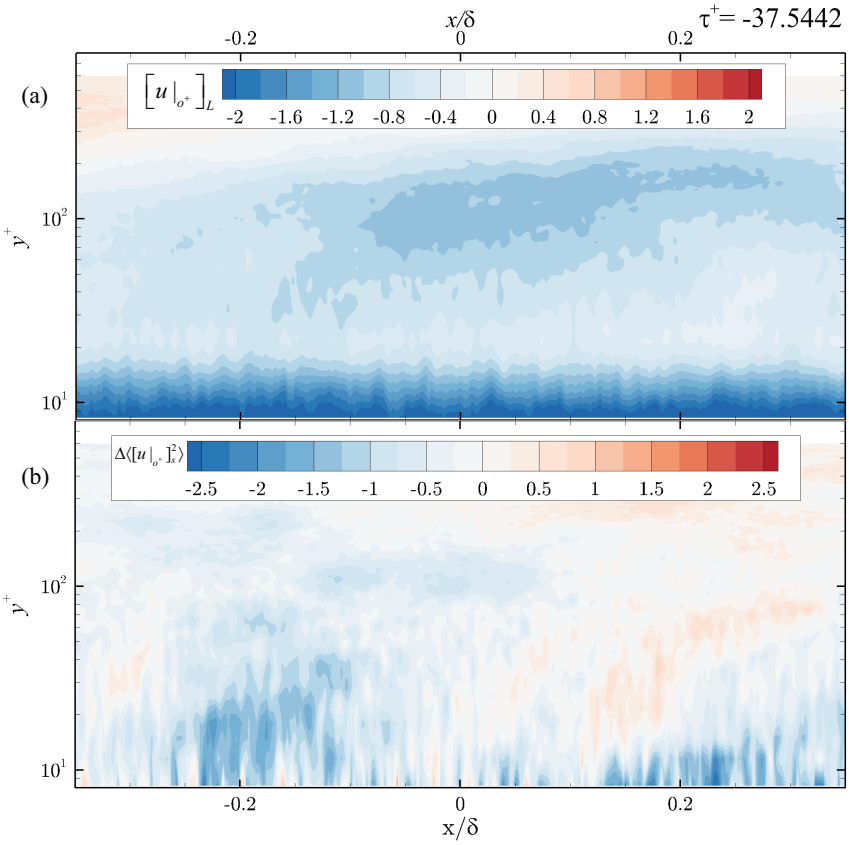

Figure 6. (a) Conditionally-averaged velocity fields of $[u|_{o^+}]_L$, and (b) corresponding small-scale energy discrepancy $\Delta\langle[u|_{o^+}]_s^2\rangle$ at $\tau \approx -37.5y^*/u_\tau$

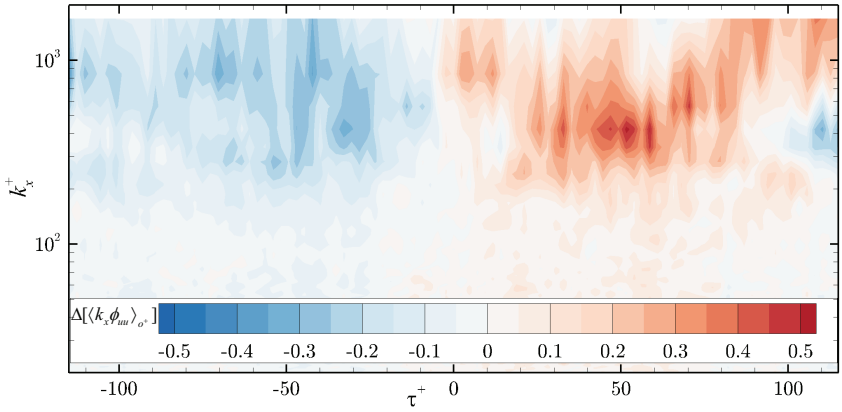

Figure 7. Discrepancy from unconditional mean of conditionally-averaged streamwise TKE spectrum, $\Delta[\langle k_x\phi_{uu}\rangle_{o^+}]$, at a wall normal position $y^+ \approx 21$

Örlü, Ramis & Schlatter, Philipp 2013 Comparison of experiments and simulations for zero pressure gradient turbulent boundary layers at moderate reynolds numbers. *Experiments in fluids* **54** (6), 1547.

Pathikonda, G. & Christensen, K. T. 2017 Inner-outer interactions in a turbulent boundary layer overlying complex roughness. *Phys. Rev. Fluids* p. (accepted for publication).

Rao, K.N., Narasimha, R. & Narayanan, M.A. 1971 The bursting phenomenon in a turbulent boundary layer. *J. Fluid Mech.* **48** (02), 339–352.

Schlatter, Philipp & Örlü, Ramis 2010 Assessment of direct numerical simulation data of turbulent boundary layers. *Journal of Fluid Mechanics* **659**, 116.

Talluru, K.M., Baidya, R., Hutchins, N. & Marusic, I. 2014 Amplitude modulation of all three velocity components in turbulent boundary layers. *J. Fluid Mech.* **746**, R1.

Zhang, C. & Chernyshenko, S. I. 2016 Quasisteady quasihomogeneous description of the scale interactions in near-wall turbulence. *Phys. Rev. Fluids* **1** (1), 014401.